CHEMISTRY OF MATERIALS
Cite This: Chem. Mater. 2018, 30, 2093−2101
Article
pubs.acs.org/cm

Experimental Validation of Ferromagnetic−Antiferromagnetic Competition in $Fe_xZn_{1-x}Se$ Quantum Dots by Computational Modeling

Jasleen K. Bindra,[†,‡] Lavrenty Gennady Gutsev,[†] Johan Van Tol,[‡] Kedar Singh,[§] Naresh S. Dalal,[†,‡] and Geoffrey F. Strouse*[,†]

[†]Department of Chemistry and Biochemistry, Florida State University, Tallahassee, Florida 32306, United States
[‡]National High Magnetic Field Laboratory, Florida State University, Tallahassee, Florida 32310, United States
[§]School of Physical Sciences, Jawaharlal Nehru University, New Delhi 110067, India

Supporting Information

ABSTRACT: Traditionally computational methods have been employed to explain the observation of novel properties in materials. The use of computational models to anticipate the onset of such properties in quantum dots (QDs) a priori of their synthetic preparation would facilitate the rapid development of new materials. We demonstrate that the use of computational modeling can allow the design of magnetic semiconductor QDs based on iron doped ZnSe prior to the preparation of the sample. DFT modeling predicts the formation of multinuclear Fe clusters within the 10% Fe doped ZnSe QD to relieve lattice strain leading to the onset of competing ferromagnetic (FM)−antiferromagnetic (AFM) interactions, or in effect spin frustration, between the local spins. The magnetic properties when iron is incorporated into a 1.8 nm ZnSe QD are computationally analyzed using standard density functional theory (DFT) simulations, and the resultant spin and Fe localization models are experimentally evaluated using SQUID, ^{57}Fe Mössbauer, and electron paramagnetic resonance (EPR) spectroscopy. The observation that the experimental results agree with the DFT predicted behavior demonstrates the value of using modeling when targeting a desired material property.

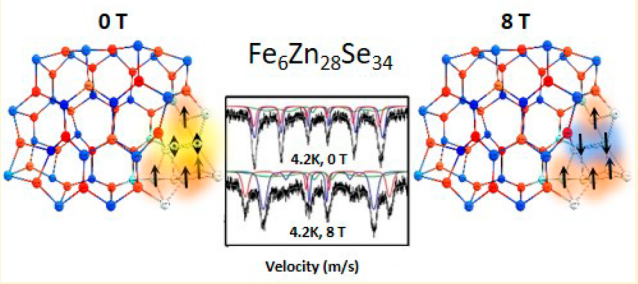

The observation of magnetic exchange in nonmagnetic semiconductors when doped with paramagnetic ions has long attracted researchers to them as potential materials for quantum computing and spintronic applications.[1−7] The onset of magnetic coupling in dilute magnetic semiconductor quantum dots (DMSQDs) is known to be dependent on the presence of carriers[3] and ion clustering.[4,8] Recent interest in iron doped II−VI lattices has arisen due to the report of unique optical and spin glass magnetic behavior.[9−13] In $ZnFe_2O_4$ spinels, the formation of interacting Fe(III) tetrahedral spin clusters due to low Fe(III) solubility was observed resulting in spin frustration analogous to Kagome lattices.[14] Similar aggregation of Fe(III) was recently observed in Fe doped ZnSe nanobelts.[8] In Fe(III)-doped ZnO, room temperature ferromagnetism was reported,[15] while in Fe doped into CdSe quantum dots (QDs) a ferromagnetic to spin glass transition at low temperature occurs.[16] The observed magnetic behavior in iron doped ZnO was accounted for by the presence of mobile carriers coupling the spin centers in the lattice, as described within the polaron percolation theory using dynamical mean-field theory (DMFT) modeling.[17] Density functional theory (DFT) while traditionally used to explain an observed property in an isolated material can also be used to predict the likelihood of spin interactions arising from iron clustering providing a route to choose a target dilute magnetic semiconductor prior to its synthesis. A recent study on iron doped CdSe clusters ($Fe_nCd_{9-n}Se_9$) reported iron center clustering can impact the magnetic interactions of the dopants.[18] With the advancement in density functional theory, computational codes are robust enough to allow even larger clusters to be modeled to ascertain the magnetic properties of a specific size and composition prior to their preparation.[18−20]

In this manuscript, we utilize the readily available DFT codes using the Generalized Gradient Approximation (DFT-GGA) to evaluate Fe doped ZnSe. DFT calculations were performed on two $(ZnSe)_{34}$ cluster models representing surface (when sliced along the ⟨0001⟩ lattice plane) and core (when sliced along the ⟨11$\bar{2}$0⟩ lattice plane) of the $(ZnSe)_{68}$ cluster which is a cluster analogue of a 1.8 nm ZnSe QD. The DFT-GGA model indicates the formation of competing ferromagnetic−antiferromagnetic (FM-AFM) interactions, or in effect spin frustration, between the local iron centers for as little as six Fe incorporated

Received: January 12, 2018
Revised: March 5, 2018
Published: March 6, 2018

DOI: 10.1021/acs.chemmater.8b00143
Chem. Mater. 2018, 30, 2093−2101

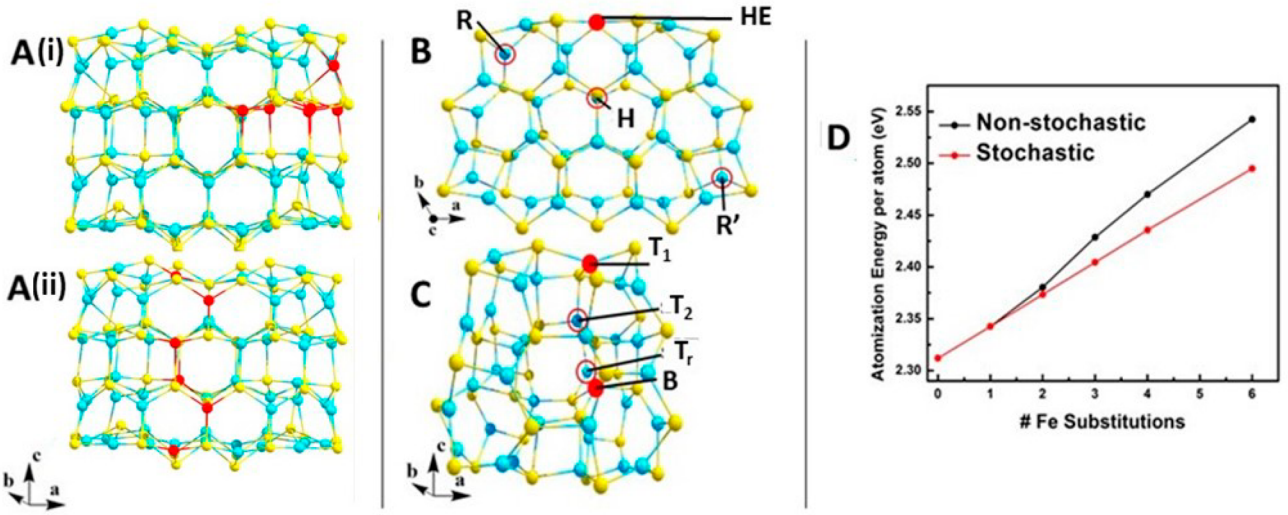

Figure 1. (A) (i) Geometry and spin energy minimized structure for the **4R′**, **2HE-2**, and the (ii) **6T$_1$- 1**[$Fe_6Zn_{62}Se_{68}$] cluster with the Se sites in yellow, Zn in blue, and Fe(III) in red. The unique sites within the cluster are labeled and shown projected along the (B) $(ZnSe)_{34}$ cluster along the ⟨0001⟩ lattice plane and (C) $(ZnSe)_{34}$ cluster along the ⟨11$\bar{2}$0⟩ lattice plane. (D) Plot of atomistic energies for increasing Fe incorporation into the cation sites in the [$Zn_{68}Se_{68}$] for a random distribution.

onto Zn sites for the $Zn_{68}Se_{68}$ cluster. The FM-AFM interactions are predicted to generate a ferrimagnetic material due to formation of spin triangles within the lattice. The prediction provided by the computational models was directly compared to experimental data on nearly analogous synthetically prepared spherical 1.8 ± 0.7 nm $Fe_{0.1}Zn_{0.9}Se$ QDs having a wurtzite structure. Temperature, field, and frequency dependent magnetic data measured by SQUID are consistent with the DFT models. Field-dependent ^{57}Fe Mössbauer further confirms the computational modeling and can be fit to the presence of two distinct sublattices that are antiferromagnetically coupled. The results of the study show that the use of readily available DFT computational approaches prior to synthesis can steer materials design when targeting dilute magnetic semiconductor quantum dots (DMSQDs).

RESULTS AND DISCUSSION

Density Functional Theory Calculations. Using DFT-GGA methods, the geometric and magnetic properties of [$Fe_nZn_{68-n}Se_{68}$] (n = 0−6) was modeled as a cluster analogue (Figure 1Ai/ii) of a 1.8 nm $Fe_xZn_{1-x}Se$ QD. The iron incorporation and resultant structural perturbation were energy minimized for sequential addition of Fe centers on Zn sites. The cluster is calculated as a neutral cluster with the Fe atom occupying a Zn site prior to energy minimization. In order to validate the DFT modeling, natural bond order (NBO) calculations were performed to analyze the bonding behavior and charge distribution. The DFT calculations indicate a charge much smaller than +2 or +3 due to the covalency of Fe−Se and Fe−Fe bonds (Supporting Information Figure SI 6). To optimize calculation time, the calculations are carried out on two smaller $(ZnSe)_{34}$ clusters representative of a surface and core of the $(ZnSe)_{68}$ cluster. The two $(ZnSe)_{34}$ clusters represent a four-layer wurtzite projection sliced along the ⟨0001⟩ projection (Figure 1B) using a 2-layer motif referred to as the boron nitride (BN) model in earlier studies and the ⟨11$\bar{2}$0⟩ direction (Figure 1C).[21] When sliced along the ⟨0001⟩ plane, the four unique cation sites are a hexagonal body (H), hexagonal edge (HE), rhombic site (R), and birhombic site (R′) (Figure 1B). In the ⟨11$\bar{2}$0⟩ slice, a tetrahedral core site (B), a tetrahedral convex (T_1) and tetrahedral concave (T_2) surface site, and a trigonal site at the cluster edges (Tr) can be identified (Figure 1C). Using these discrete sites, a simple naming protocol is implemented to distinguish the Fe occupation site, number of Fe atoms at the site, and layer for the inclusion ({no. ions × site} − layer). The **(4R′-2HE-2)** motif (projected in Figure 1A(i)) has six Fe where four ions occupy the birhombic R′ site and two occupy the hexagonal edge (HE) site sitting on the internal second layer of the cluster. The **(6T$_1$-1)** structure (Figure 1A(ii)) corresponds to six Fe ions occupying tetrahedral convex sites at the surface of the cluster.

As the Fe center is introduced into the lattice, geometric and electronic changes arise due to lattice strain and the low solubility of Fe in ZnSe.[22] The magnitude of the geometric effect will depend on the site of occupation. The Fe can exist as single ion defects (occupying core sites within the lattice or surface bound sites) or form pairs or higher nuclearity clusters on antisites. Antisite pairs are anticipated to result in large local geometry distortion to minimize energy. The favorability of substitution of Fe onto the tetrahedral Zn cation site in ZnSe is calculated from the binding energy per atom (E_b)

$$E_b = \frac{[xE_{at}(\mathrm{Zn}) + mE_{at}(\mathrm{Se}) + nE_{at}(\mathrm{Fe})] - E(\mathrm{Zn}_x\mathrm{Se}_n\mathrm{Fe}_m)}{2n}$$

where x, n, and m are the number of Zn, Fe, and Se atoms, respectively. E_{at} is the atomization energy in eV to yield a value of E_b in eV/atom.

The lowest energy geometry-optimized structures for six iron incorporations are shown in Figures 1A for **(4R′-2HE-2)** and **(6T$_1$-1)** motifs. The DFT minimized structures for Fe incorporation at all possible sites for interacting and non-interacting Fe centers into [$Fe_nZn_{34-n}Se_{34}$] (n = 1, 2, 3, 4, 6) are available in Supporting Information Figures SI 2−7. The energy difference between clustered and nonclustered incorporation of Fe with increasing number of iron atoms in [$Fe_nZn_{34-n}Se_{34}$] can be seen by inspection of Figure 1D. With increasing Fe content, the energetics for incorporating Fe

DOI: 10.1021/acs.chemmater.8b00143
Chem. Mater. 2018, 30, 2093−2101

randomly onto the cation sites suggests a nonstochastic distribution of Fe ions within the lattice is energetically favorable for $n \geq 3$. Substitution at non-neighboring Zn sites is less favorable by 0.024 eV/atom, 0.034 eV/atom, and 0.047 eV/atom in the case of three, four, and six Fe-substitutions, respectively. A value of $n = 3$ corresponds to 5% doping of the cations in a 1.8 nm QD. Energetically the observation of increase in nuclearity with each substitution is not surprising, as the solubility of Fe in ZnSe is low[22] and previous studies have empirically suggested doping of aliovalent ions into a II−VI lattice will lead to clustering to lower lattice strain and compensate for charge.[8,14,23]

For a single Fe ($n = 1$), the calculated energies for cation site substitution are in the order $T_r < T_1 < B < T_2$ in $\langle 11\bar{2}0 \rangle$; while for $\langle 0001 \rangle$ the order is R′ < R < H < HE. Substitution at the birhombic R′ site is energetically most favorable by approximately ∼0.02 eV relative to the other sites. In the case of $n = 2$, all possible Fe sites in $[Fe_2Zn_{32}Se_{34}]$ producing 20 geometrically distinct models were considered, including spin multiplicities M between 1 and 9 ($M = (2S + 1)$). The lowest energy configuration occurs for the cluster **H-21** (21 indicates that the first substitution is on the bottom layer and the second one is on the top layer) having a $M = 9$. In this configuration, the iron atoms move toward one another by 1.0 Å favoring Fe−Fe pairing when incorporated into the lattice. Note, the non-neighboring substitutions (>3.5 Å separation) are higher in energy by 0.61 eV. For three substitutions ($n = 3$) there are 34 possible Fe sites of incorporation to be considered. The lowest energy motif is for the states with triple birhombic substitution geometry **3R′** with M = 11. The **3R′** motif is significantly lower in total energy for all spin multiplicities than the states of its energetically closest neighbors. For **3R′**, more spin density is localized on a Se shared by the three Fe centers, resulting in favorable Fe−Fe interactions. For $n = 4$, the lowest energy motif occurs for **4R′** ($M = 9$) where the Fe ions cluster and form a defined tetrahedron where three of the total Fe spins are up and the fourth is down, creating frustration in the spin−lattice. Although not calculated, similar results are expected for $n = 5$.

For $n = 6$, the relative energies for the lowest energy structures, the surface localized **(6T$_1$-1)**, and the internal inclusion **(4R′-2HE-2)** motifs are shown in Figure 2A. The spin projections are shown for **(4R′, 2HE-2)** ($M = 1$, 3, 9, 15, and 23) and for **(6T$_1$-1)** ($M = 1$, 3, 7, 13) in Figure 2B,C. The bold arrows in Figure 2 represent the spin direction for each Fe ion. The energy minimum for the $n = 6$ Fe inclusion occurs at $M = 1$ and 3 for **(4R′, 2HE-2)** and at $M = 3$ for **(6T$_1$-1)**. The spin configuration in **(6T$_1$-1)** is +0.26 eV higher in energy than in the **(4R′, 2HE-2)**, suggesting formation of an inclusion at the surface. The M = 1 and 3 spin motifs in **(4R′, 2HE-2)** are anticipated to result in competitive AFM-FM spin interactions that may lead to a spin frustrated system arising from the combination of two distinct AFM coupled sublattices, reminiscent of a Kagome lattice arrangement.[24]

Evaluating the DFT Model. The expected evolution of an interacting magnetic sublattice in $Fe_nZn_{1-n}Se$ QDs arising from the formation of iron clusters occupying sites similar to the lowest energy DFT-GGA can be evaluated for synthetically prepared 1.8 nm $Fe_xZn_{1-x}Se$ QDs ($x = 0.01$, 0.05, 0.1). The samples were prepared using a single source cluster based doping protocol previously established by our lab.[25] Due to the difficulty in TEM imaging of ZnSe (low z-number), complete characterization data (TEM, pXRD, ICP-MS) is provided for

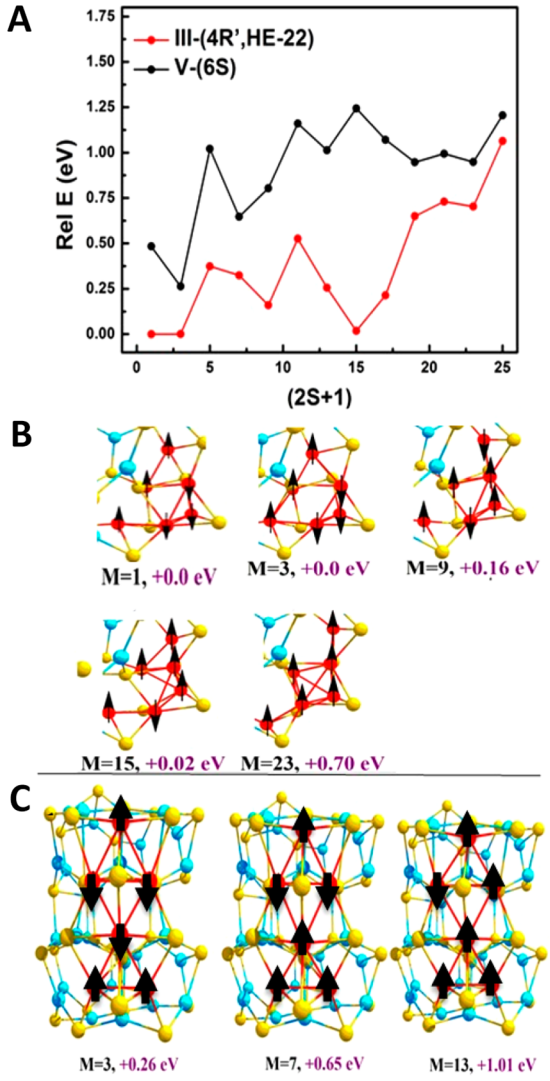

Figure 2. (A) Plot of relative energy vs spin multiplicity for 4R′, 2HE-2, and 6T1-1 clusters. (B and C) Structural projections identify the individual Fe substitutional site and spin orientation.

$Fe_{0.1}Zn_{0.9}Se$, while selected data is provided for the other samples (Supporting Information Figures SI 8 and SI 9). The Fe(III) doping levels are validated by ICP-MS (Table SI 1). Iron doping corresponds to an on-average incorporation of one Fe(III) center at 1%, three at 5% and six at 10%.

For the $Fe_{0.1}Zn_{0.9}Se$ sample, the TEM images reveal spherical particles with a size distribution of 1.8 ± 0.7 nm for a limited sample size. The structure of the QD is wurtzite based on pattern fitting of the pXRD data. Scherrer broadening analysis of pXRD data average crystallite size agrees with the TEM image (1.8 nm) for $Fe_{0.1}Zn_{0.9}Se$. Scherrer analysis of the other samples was therefore used to assign the size of the $x = 0.01$ and 0.05 samples to 1.8 nm (Supporting Information Figure SI 8).

Fe(III) Site Analysis. In the prepared $Fe_xZn_{1-x}Se$ QDs where $x = 0.01$, 0.05 and 0.1, the site of occupation of the iron centers is assigned by analysis of high frequency electron paramagnetic resonance (HF-EPR, 240 GHz). The EPR spectra were measured on powdered samples for $Fe_xZn_{1-x}Se$ at room temperature. For the three samples, the HF-EPR data in Figure 3A exhibit two overlapping Lorentzian absorption features with distinct g-values. The observed spectra are broad with respect

DOI: 10.1021/acs.chemmater.8b00143
Chem. Mater. 2018, 30, 2093−2101

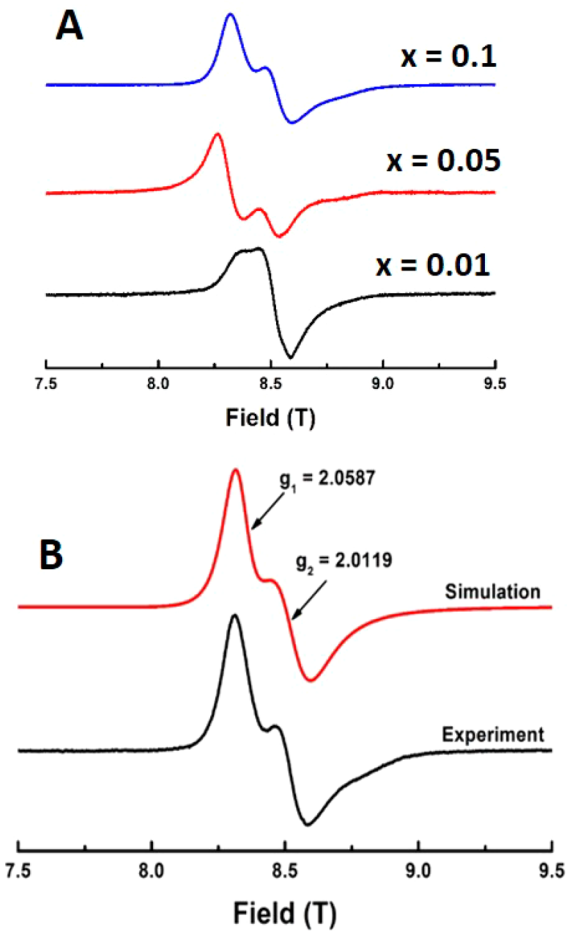

Figure 3. (A) Concentration dependence HF-EPR (240 GHz) of 1.8 nm, $Fe_xZn_{1-x}Se$ (x = 0.1, 0.05, 0.01) at 290 K. (B) Simulated (red) and experimental (black) HF-EPR (240 GHz) spectra, for 1.8 nm $Fe_{0.1}Zn_{0.9}Se$ at 290 K.

to what you might expect for Fe(III) impurities. This might be due to strong crystal strain and/or dipolar and exchange coupling.

The EPR is assigned to Fe(III) centers in the QD and consists of two prominent features whose intensity is concentration dependent. In the Supporting Information Figure SI 10 the full frequency sweep for the 5% Fe sample is shown between 0 and 12T, where no new features are observed, as would be expected for the presence of an octahedral species (g = 4.2, signal at H = 4.08 T at 240 GHz).[26]

Figure 3B shows simulated and experimental spectra for $Fe_{0.1}Zn_{0.9}Se$. The EPR spectral components can be simulated by two overlapping spectral components arising from two unique Fe(III) centers (S = 5/2, I = 0 ground state) in the QD samples. From the simulations of the EPR spectra g_1 ($g_1 \sim$ 2.045) is observed to be the dominant site and is invariant with iron concentration, while the g_2 value is dependent on the concentration of iron ($g_2^{x=0.01}$ = 2.0587, $g_2^{x=0.05}$ = 2.02687, $g_2^{x=0.1}$ = 2.0119). The intensity for site 2 (g_2) to the EPR spectra increases with increasing Fe(III) content in Figure 3.

Two Fe(III) sites have been observed by EPR by Singh et al. and Singhal et al. for iron doped CdSe and iron doped indium oxide nanoparticles, although the nature of the sites was not analyzed.[16,27] In comparison Watanabe observed by single crystal measurements on iron doped II−VI systems that the EPR was assigned as Fe(III) on a tetrahedral site with an associated V_{cation} pair site.[28] The two g values are assigned as a normal cubic symmetry T_d site (g_1 = 2.0587) and a trigonally distorted T_d site (g_2 = 2.0119) based on comparison to the literature.[26−29] The observation of two g values in the EPR data is consistent with the DFT predictions for (**4R′, HE-22**) where the pair of iron centers was observed to occupy two unique sites that are distorted from pure T_d symmetry by relaxation of the Fe−Fe by 1.0 Å toward each other in the modeled cluster.

Magnetic Susceptibility. The temperature dependent AC and DC magnetic susceptibilities for the 1.8 nm $Fe_xZn_{1-x}Se$ QDs (x = 0.01, 0.05, and 0.1) are shown in Figure 4. DC susceptibility measurements on the $Fe_xZn_{1-x}Se$ samples (Figure 4A−C) are complex, exhibiting multiple magnetic transitions. Concentration dependent divergence between ZFC and FC data is observed at 100 K for x = 0.01, 120 K for x = 0.05, and 175 K for x = 0.10 $Fe_xZn_{1-x}Se$ samples. A lower temperature AFM transition below 25 K is observed in all samples. This allows the assignment of two magnetization events occurring at <25 K and one between 25 and 175 K. The observed complex magnetic data can be interpreted in terms of a competitive FM and AFM coupling coexisting in the sample, and the experimental observation of coercivity extracted from the ratio of FC to ZFC data supports the existence of two coupled magnetic transitions (Supporting Information Figure SI 11).

To analyze the magnetic transitions and the presence of superparamagnetic (SPM) or spin glass type behavior in the $Fe_xZn_{1-x}Se$ samples AC susceptibility measurements were carried out (Figure 4D−I). The AC data clearly distinguishes two transitions, a frequency independent transition below 50 K and a frequency dependent transition above 100 K. Fitting of the frequency dependent transition to the Mydosh criteria[30] yields a Mydosh parameter (Φ) value of 0.16 for x = 0.01 indicating SPM behavior at low dopant concentrations. While Φ = 0.04 for the x = 0.05 and Φ = 0.02 for the x = 0.10 sample attributes to spin glass type behavior in samples with high dopant concentrations. The appearance of spin-glass behavior for concentrations above 5% is consistent with the enhanced pairing predicted by DFT modeling leading to the observed concentration dependent freezing temperature above 100 K.

The relaxation rate can be extracted from the out-of-phase component of the temperature-dependent AC susceptibility measurements. Figure 4G−I can be fit to the Arrhenius equation

$$\tau = \tau_0 \exp\left(\frac{E_a}{k_B T}\right)$$

where τ is the average relaxation time, calculated by $(1/(2\pi\nu))$, where ν is the frequency of the AC measurement, τ_0 is the characteristic reversal attempt time, and E_a/k_B is the magnetic barrier energy. The data extracted from the Arrhenius plot confirms SPM behavior at x = 0.01 with E_a/k_B = 263 ± 33 K and $\tau_0 = 4.3 \times 10^{-7}$ s, while unphysical values of E_a/k_B and τ_0 for x = 0.05 and 0.1 (Supporting Information Table SI 2) are consistent with spin glass behavior. Similar field-dependent non-Langevin magnetization with a tangential loss in the AC-magnetic susceptibility indicating SPM was also observed in previous studies of Mn doped CdSe.[31] The observation of spin glass behavior in the $Fe_xZn_{1-x}Se$ QDs is consistent with earlier reports for Fe(III) incorporation in II−VI materials.[15,26] The results for the $Fe_{0.1}Zn_{0.9}Se$ QDs can be compared to the structural model predictions from DFT, allowing that the

DOI: 10.1021/acs.chemmater.8b00143
Chem. Mater. 2018, 30, 2093−2101

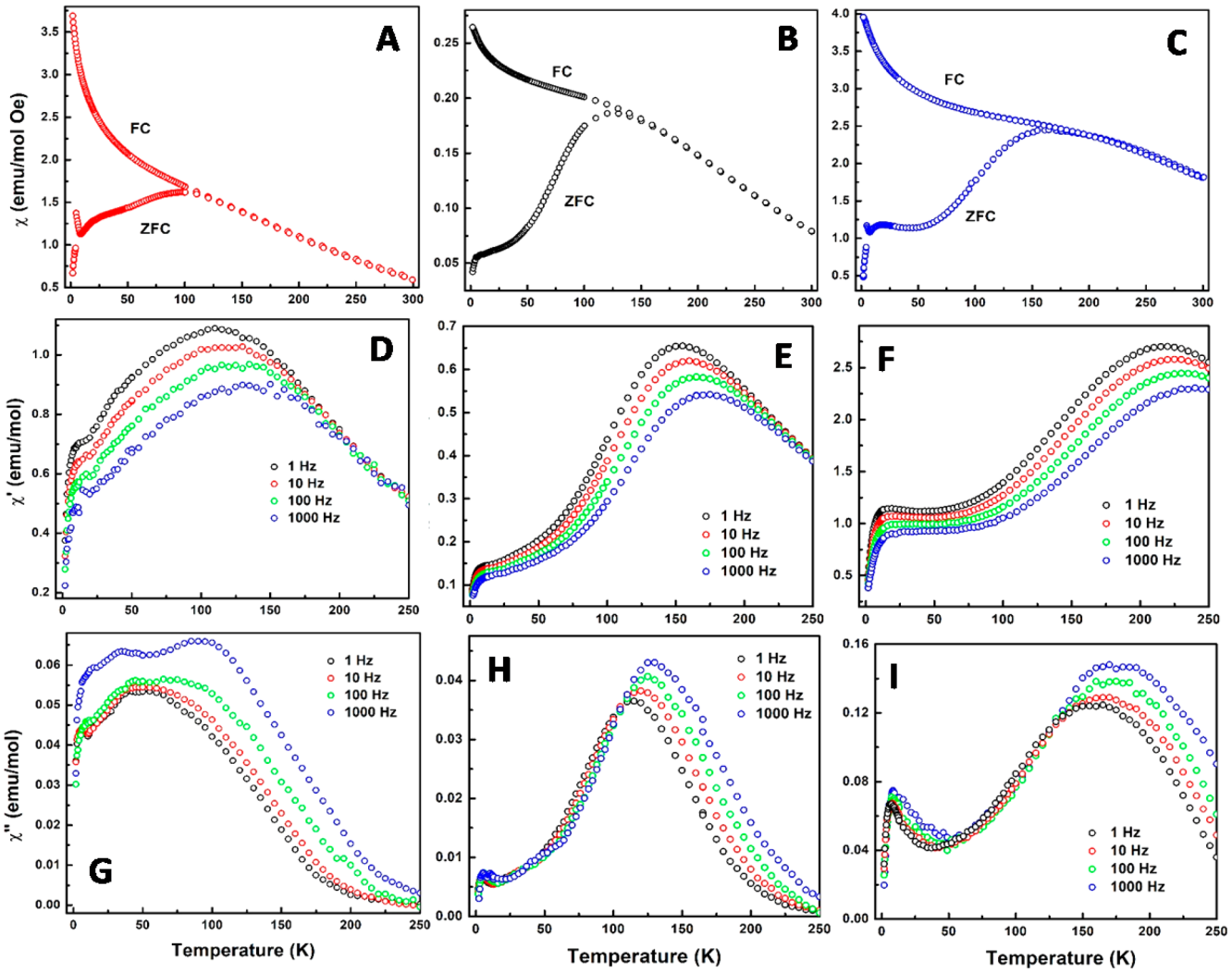

Figure 4. DC-SQUID susceptibility, FC and ZFC plots for 1.8 nm, and $Fe_xZn_{1-x}Se$ where x = 0.01 (A), 0.05 (B), and 0.1 (C). AC susceptibility in-phase plots for x = 0.01 (D), 0.05 (E), and 0.1 (F) and AC susceptibility out-of-phase plots for x = 0.01 (G), 0.05 (H), and 0.1 (I) in 1.8 nm $Fe_xZn_{1-x}Se$ quantum dots.

frequency independent transition is assigned to an antiferromagnetic transition with a Néel temperature T_N = 4.83 K. The experimental results are consistent with the presence of two interacting spin lattices, which is consistent with the DFT-GGA spin motif as shown for the **(4R′-2HE-2)** n = 6 motif.

Effective Magnetic Moment. In **(4R′-2HE-2)**, a μ_{eff} of 2.83 is anticipated for M = 1 and 3. The temperature dependent (1.8−300 K) effective magnetic moment ($\mu_{eff} = (8\chi T)^{1/2}$) for the $Fe_xZn_{1-x}Se$ samples is plotted in Figure 5A in units of Bohr magnetons. A diamagnetic correction to the experimental data was calculated using Pascal constants.[32] The μ_{eff} value decreases at lower temperatures suggesting the onset of partial ordering. The μ_{eff} for $Fe_{0.1}Zn_{0.9}Se$ at 298 K is 4.72 μ_β, which is close to the spin-only value for S = 1−1.5, since $\mu_{eff} = g^2S(S+1)$ when g = 2.0. The agreement in μ_{eff} is reasonable, as only the two lowest energy states are considered. Concentration dependence of μ_{eff} was analyzed by calculating and comparing μ_{eff} for different Fe concentrations in $Fe_xZn_{x-1}Se$ where x = 0.01, 0.05, and 0.1. As shown in Figure 5, μ_{eff} decreases exponentially with increase in concentration. This supports AC-SQUID measurements which indicate that increase in concentration leads to the formation of local geometries leading to the decrease in μ_{eff}.

Mössbauer Measurements. To assess the validity of the DFT modeling that predicts strong FM-AFM competitive interactions for the $Fe_{0.1}Zn_{0.9}Se$ sample, field- and temperature-dependent ^{57}Fe Mössbauer spectra were recorded for a 100% ^{57}Fe-enriched sample of the $Fe_{0.1}Zn_{0.9}Se$ QDs (Supporting Figure SI 12). The 4.2 K, 0 T spectrum exhibits a slightly asymmetric sextet with a magnetic hyperfine splitting corresponding to an internal field of B_0 = 51.4(5) T and a Gaussian distribution in hyperfine fields described by a full width at half-maximum (fwhm) dB = 4.2(5) T. This component exhibits an apparent isomer shift, δ = 0.45(3) mm/s, and a vanishing quadrupolar perturbation, ε = 0.00(8), along the direction of the internal field. Moreover, this component accounts for only ∼75(4)% of the iron present in the sample. The remaining amount is associated with a broadly distributed, heterogeneous spectral component. Inspection of Figure 6A shows that the applied magnetic field induces the splitting of the zero-field sextet into two subcomponents. While the major component exhibits a linearly dependent decrease, the minor component exhibits an increase of their magnetic hyperfine splitting with increasing strength of the applied field (a slope of +0.93/−0.91 for the major/minor component); see Figure 6B. The observed behavior suggests that the internal

DOI: 10.1021/acs.chemmater.8b00143
Chem. Mater. 2018, 30, 2093−2101

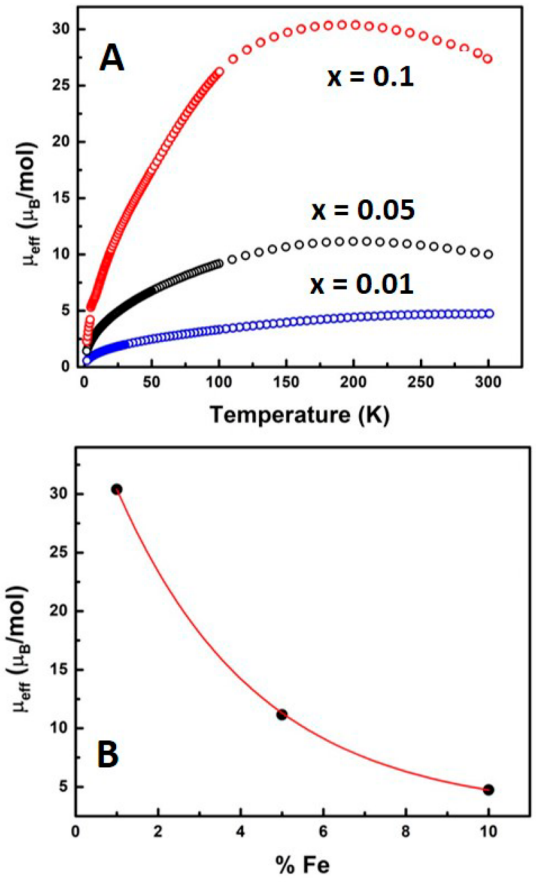

Figure 5. (A) μ_{eff} plots for 1.8 nm, $Fe_xZn_{1-x}Se$ (x = 0.1, 0.05, 0.01). (B) Exponential decrease in μ_{eff} with increase in Fe concentration.

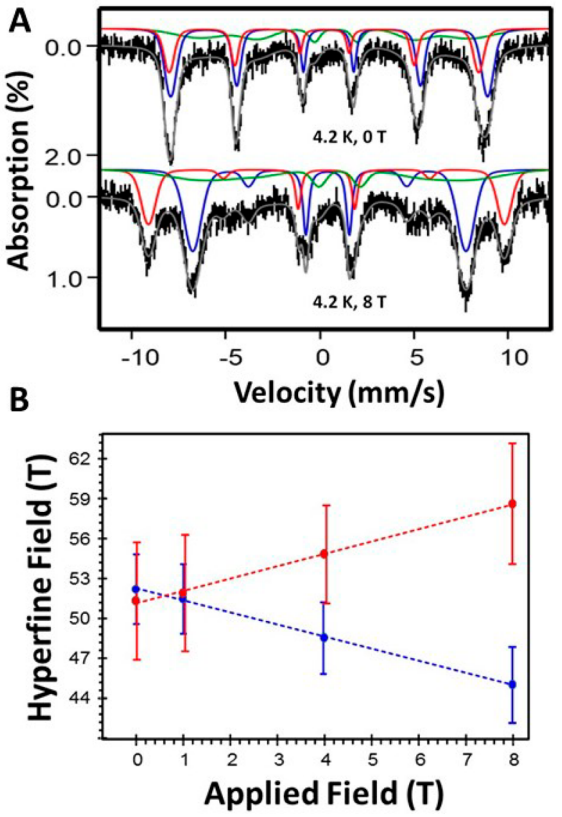

Figure 6. (A) Field-dependent ^{57}Fe Mössbauer spectra recorded at 4.2 K for the 1.8 nm, dodecylamine-passivated $^{57}Fe_{0.1}Zn_{0.9}Se$ nanoparticles. (B) The dependence of the internal field on the applied field determined at 4.2 K for the two distinct Fe(III) spectral components. The magnitude of the error bars is determined by the width (dB [T]) of the Gaussian HFD of the respective spectral component.

field of the major component aligns antiparallel and that of the minor component parallel to the applied field revealing an antiferromagnetic coupling between the two magnetic sublattices.[33] This behavior also allows us to deconvolute the individual components of the zero-field spectrum including that associated with the heterogeneous component; see Supporting Information Table SI 4. The observed parameter values of the two sextet subcomponents, of the isomer shifts, are typical of high-spin Fe(III) ions and suggest that most of the doped iron ions are found as Fe(III).[34] The disordered phase cannot be definitively assigned as Fe(III) or Fe(II), nor can the site or location of the disordered iron centers be clearly identified. While it would be convenient to assign the disordered iron centers to surface contributions, the disordered iron centers cannot be assigned as core or surface, as the surface of a 1.8 nm QD accounts for ~80% of the QD if a spherical geometry is assumed.

The zero-field, temperature-dependent spectra recorded for this sample are indicative of a SPM behavior (Supporting Information Figure SI 13). Thus, the 293 K, 0 T spectrum consists of a sextet superimposed over a quadrupole doublet (Supporting Information Figure SI 13). The quadrupole doublet accounts for ~20% of the spectral area and is best described using an isomer shift δ = 0.14(5) mm/s, a quadrupole splitting ΔE_Q = 0.50(5) mm/s, and a line width Γ = 0.45(5) mm/s. The sextet and the doublet are associated with a QD for which their magnetic moment relaxes slower and, respectively, faster than the rate of the nuclear Larmor precession ($\omega = 10^6$ s^{-1}).[35−37] Moreover, the temperature-induced decrease in the magnitude of the magnetic hyperfine splitting of the sextet can be associated with the occurrence of collective magnetic excitations. While the effect can also arise from interactions between QDs, carrying out the Mössbauer measurements diluted in eicosane will substantially reduce the effect of this contribution in this study.

Comparison of the Mössbauer and DFT Model. The observed experimental Mössbauer values obtained for the 1.8 nm $Fe_{0.1}Zn_{0.9}Se$ in Supporting Information Table SI 4 can be directly compared to what would be predicted for Mössbauer results from the DFT (**4R′**, **2HE-2**) and (**6 T_1-1**) cluster models by calculating the isomer shift (δ) and hyperfine coupling (A_{ij}) values using the computational method of Bochevarov et al.[38] The Mössbauer isomer shift and isotropic hyperfine constants are calculated using the high spin, intermediate spin, and parallel and antiparallel spin alignments in $[Fe_6Zn_{62}Se_8]$. According to Bochevarov, when using the BPW91/Partridge-1 basis set[39] the Mössbauer isomer shift (δ) is related to the DFT derived electron density at the nucleus (ρ), such that $\delta_{DFT} = -0.354372\rho + 4194.389259$. The hyperfine constant (A_{ij}) can then be calculated from the derived δ value and electron density ($\rho^{\alpha-\beta}$), $A_{ij}^{K,contact} = \delta_{ij}\frac{8\pi}{3}\frac{g_e g_K \beta\beta_K}{2S}\rho^{\alpha-\beta}(R_K)$,where g_e is the free-electron g factor (= 2.0023) and β is the Bohr magneton, g_K and β_K are the nuclear g factor and nuclear magneton of the Kth nucleus, respectively, and $\rho^{(\alpha-\beta)}(R_K)$ is the contact electron spin density at nucleus K. Comparison of the computational value with

DOI: 10.1021/acs.chemmater.8b00143
Chem. Mater. 2018, 30, 2093−2101

experimental data is accomplished by applying the scaler A_{exptl} which is $1.81A_{DFT}$ and the conversion factor $\frac{A}{g_{K\beta_K}} = 0.7238T$ to convert from units of MHz to Tesla (T).

Following from the approach of Bochevarov et al.,[38] the lowest energy spin projections for **(4R′, 2HE-2)** that yield calculated isomer shifts (δ) would be 0.57 mm/s for S = 1 and 3 and 0.47 mm/s for S = 15, and the isotropic hyperfine constants (A) are 47.79 T for S = 1, 51.42 T for S = 3, and 7.26 T for S = 7. For **(6 T_1-1)**, the calculated isomer shifts (δ) are 0.56 mm/s for S = 3 and 0.66 mm/s for S = 7 and the isotropic hyperfine constants (A) are 58.40 T for S = 3 and 14.84 T for S = 7 (Supporting Information Table SI 3).

The experimentally measured and computational predicted Mössbauer parameters for the spin clusters and the QD sample are in remarkable agreement. Notably, the experimental data for the QD is the same as the calculated values for the spin cluster **(4R′, 2HE-2)** suggesting that the presence of antiferromagnetic and ferromagnetic interactions coexisting within the lattice would lead to spin frustration.

■ CONCLUSIONS

In materials chemistry and physics, the classical approach is to explain experimental measurements by computational modeling using simplified structural motifs due to the constraints of the code. The enhancement of code allows an opportunity to use computational methods to provide guidance on synthesis to target a specific material property rather than merely conformation of results. The continued advancement of computational methods will soon reach a point where the potential materials targets for quantum computing, spintronics, and optoelectronic materials can be evaluated prior to synthetic preparation. The coupling of in silico predictions provides guidance in designing a synthetic target to isolate a new class of dilute magnetic semiconductor quantum dots (DMSQDs) representing an important breakthrough in the field.

DFT-GGA methods are employed to identify the doping level of Fe(III) in ZnSe where the onset of competitive AFM-FM interactions is predicted to arise between Fe(III) centers due to clustering within the ZnSe QD lattice. The results of the DFT compared to experimental measurements support the concept of using advanced DFT calculations. The impact of the use of DFT-GGA codes in developing DMSQD targets may lead to a new approach to design effective synthetic libraries to speed discovery in DMSQDs, an approach reminiscent of strategies employed for discovery for pharmaceutical research.

■ EXPERIMENTAL SECTION

Chemicals. Dodecylamine (DDA) (90%, Acros Organics), $FeCl_3$, (99.9% Acros Organics), ^{57}Fe powder (Cambridge Isotopes), HCl (37%, Sigma-Aldrich), toluene (99.9%, EMD Chemicals), and methanol (99.8%, VWR) were used as supplied. $Li_4[Se_4Zn_{10}(SC_6H_5)_{16}]$ (Zn_{10} cluster) was prepared as previously described.

Synthesis. Dodecylamine (DDA) passivated $Fe_xZn_{1-x}Se$ QDs (x = 0.01, 0.05, and 0.1) were prepared by lyothermal growth of the doped QD using $Li_4[Se_4Zn_{10}(SC_6H_5)_{16}]$ in the presence of the transition metal salt ($FeCl_3$).[25]

Briefly, the QDs were prepared by the dissolution of $Li_4[Se_4Zn_{10}(SC_6H_5)_{16}]$ in ∼20 mL of HDA at 110 °C under N_2 using a Schlenk line. To the solution 1, 5, and 10 mol % of $FeCl_3$ was added, and the reaction was allowed to stir vigorously for 1 h to induce cation exchange between the Zn^{2+} of the cluster and the Fe(III) from the metal salt. The reaction was then heated to 210 °C (50 °C/min) to induce QD growth. The temperature was kept below 220 °C to avoid sulfur incorporation. The size of the QDs was monitored using UV−vis spectroscopy. Once the desired size was achieved, the solution was cooled to room temperature to halt further growth. The cooled solid samples were then isolated by dissolving in ∼10 mL of toluene, followed by precipitation with ∼15 mL of MeOH and centrifugation. This process was repeated three times to ensure reagent free particles, and the precipitate dried under a vacuum at room temperature. Sequential dissolution/precipitation steps have been shown to effectively remove unreacted Fe impurities. To generate ^{57}Fe doped ZnSe for Mössbauer studies, $^{57}FeCl_3$ was used as the dopant source. The metal salt was synthesized using ^{57}Fe powder and HCl in MeOH.

Magnetic Susceptibility Measurements. Magnetization measurements were conducted on 1.8 nm $Fe_xZn_{1-x}Se$ doped ZnSe QDs using a Quantum Design superconducting quantum interference device (SQUID) magnetometer. Zero field cooled (ZFC) and field cooled (FC) measurements were performed under a constant field of 100 Oe over the temperature range of 1.8−300 K. Isothermal field dependent magnetization measurements were conducted with magnetic field varying between 0 to 7 T at 1.8 K.

Electron Paramagnetic Resonance. High frequency (240 GHz) EPR measurements were conducted at the Florida State University National High Magnetic Field Laboratory (FSU-NHMFL) in Tallahassee, FL. The superheterodyne quasi-optical spectrometer operates at 120, 240, and 336 GHz and is described elsewhere. A multifrequency high-field pulsed electron paramagnetic resonance/electron−nuclear double resonance spectrometer was used.[40,41] Spectral simulations were performed using the computer program SPIN.

Mössbauer Spectroscopy. The ^{57}Fe Nuclear Gamma Resonance (Mössbauer) spectra were recorded using a spectrometer fitted with a Janis 8DT Super Varitemp flow-type cryostat cooled with liquid helium. The cryostat had a built in 8 T, American Magnetics superconducting magnet. The spectrometer was operated in a constant acceleration mode and used a light source that consisted of 100 mCi ^{57}Co dispersed in a Rh metal foil. This instrument allowed for recording spectra for temperatures 4.2−298 K and applied fields from 0 to 8 T at 4.2 K. The external field was applied parallel to the incident γ-radiation. The absorbers used in this study were obtained by dispersing 10−15 mg of iron-doped ZnSe QDs in ∼50 mg of eicosane that was gently warmed to 40 °C followed by cooling to RT. This procedure allowed us to investigate samples that were magnetically dilute, which were solid at room temperature and thus were easy to handle. These absorbers were contained in custom-made Delrin or polyethylene containers. The large nonresonant absorption of the 14.4 keV photons by the Zn and Se nuclei required us to use ^{57}Fe isotopically enriched absorbers. The isomer shift values are reported against the room-temperature centroid of a standard α-Fe metal foil. The experimental spectra were analyzed using the WMOSS software (See Co., formerly Web Research Co., Edina, MN) in the framework of the Voigt-based model developed by Rancourt et al.[42] This approach allows for the description of an arbitrary hyperfine field distribution (HFD) in terms of a discrete sum of individual Gaussian components. Each Gaussian component can be understood as originating from a large sum of elemental spectra with intensities that follow a Gaussian distribution and differ from one another in the values of a particular parameter. Furthermore, each Gaussian component is defined by three parameters, namely, p [%], a weight factor which, assuming identical f-recoilless fractions, represents the fraction of the total iron amount that is accounted for by the respective component. Furthermore, B_{obs} [T] and dB [T] account for the centroid and the width of the Gaussian HFD. In zero-field the B_{obs} [T] denotes the B_0 of the respective component. Several additional parameters are used to describe the elemental sextet spectra comprising the HFD: Γ, the full width at half-maximum (fwhm) of the intrinsic Lorentzian line shape; δ, the isomer shift; ε, the electric field gradient (EFG) tensor component along the internal field; and h_1/h_3 and h_2/h_3, the height ratios of the outer (1, 6) lines to the inner (3, 4) lines and of the middle (2, 5) lines to the inner (3, 4) lines, respectively.

DOI: 10.1021/acs.chemmater.8b00143
Chem. Mater. 2018, 30, 2093−2101

DFT-GGA Computational Methods. The two-layer and four-layer wurtzite models has been employed to theoretically validate mass spectrometry results on magic number clusters in ZnSe. In the DFT calculations the spin-polarized density functional theory (DFT) calculations were performed using the GAUSSIAN 09 suite of programs.[43] The BPW91 exchange-correlation functional, which is composed of Becke exchange[44] and Perdew–Wang correlation,[45] was used. All atoms were treated at the all-electron level using the 6-311+G* basis set of triple-ζ quality in the case of Zn[46] and Def2-TZVP for Fe ($(^{10}s^7p^4d^1f)$ and Se($^{10}s^7p^4d^1f$).[47] The convergence threshold for total energy was set to 10^{-8} eV and force threshold was set to 10^{-3} eV/Å. Test studies have shown that the BPW91 method provides a mean unsigned error in atomization energies which is similar to the errors obtained when using more recently developed exchange-correlation functionals.[48]

■ ASSOCIATED CONTENT

Supporting Information

The Supporting Information is available free of charge on the ACS Publications website at DOI: 10.1021/acs.chemmater.8b00143.

Further details of DFT-GGA computational methods, magnetic data, Mossbauer data, and materials characterization data are provided in Figures SI 1–13 and Tables SI 1–4 (PDF)

■ AUTHOR INFORMATION

Corresponding Author

*(G.F.S.) E-mail: strouse@chem.fsu.edu.

ORCID

Lavrenty Gennady Gutsev: 0000-0002-9679-9093

Naresh S. Dalal: 0000-0002-9996-6918

Geoffrey F. Strouse: 0000-0003-0841-282X

Author Contributions

The manuscript was written through contributions of all authors. All authors have given approval to the final version of the manuscript. J.K.B. prepared and measured the properties of the synthesized QD. L.G.G. performed the GFT-GGA calculations. S.S. carried out the Mössbauer measurements and H.V.T. the EPR measurements. N.S.D. and K.S. analyzed the EPR and magnetic properties. G.F.S. designed the project and assisted in interpretation, conclusions, and writing of the manuscript.

Notes

The authors declare no competing financial interest.

■ ACKNOWLEDGMENTS

We (G.F.S) wish to thank the National Science Foundation CHE-1608364: SusChEM: Understanding Microwave Interactions to Control Magnetic Nanocrystal Growth from a Single Source Precursor. K.S. and N.S.D. wish to acknowledge the Raman Fellowship for financial support. We thank Dr. Stoian for analysis of the Mössbauer parameters. The high-field EPR (Dr. Hans von Tol) and Mössbauer (Dr. Sebastian Stoian) measurements were made at the National High Magnetic Field Laboratory, which is supported by the National Science Foundation via Cooperative Agreement No. DMR-1157490 and the State of Florida. The authors declare no competing financial interests.

■ REFERENCES

(1) Lent, C. S.; Tougaw, P. D. A device architecture for computing with quantum dots. *Proc. IEEE* **1997**, *85* (4), 541–557.

(2) Shcherbakov, M. R.; Vabishchevich, P. P.; Shorokhov, A. S.; Chong, K. E.; Choi, D.-Y.; Staude, I.; Miroshnichenko, A. E.; Neshev, D. N.; Fedyanin, A. A.; Kivshar, Y. S. Ultrafast all-optical switching with magnetic resonances in nonlinear dielectric nanostructures. *Nano Lett.* **2015**, *15* (10), 6985–6990.

(3) Zheng, W.; Strouse, G. F. Involvement of carriers in the size-dependent magnetic exchange for Mn: CdSe quantum dots. *J. Am. Chem. Soc.* **2011**, *133* (19), 7482–7489.

(4) Zheng, W.; Singh, K.; Wang, Z.; Wright, J. T.; van Tol, J.; Dalal, N. S.; Meulenberg, R. W.; Strouse, G. F. Evidence of a $ZnCr_2Se_4$ Spinel Inclusion at the Core of a Cr-Doped ZnSe Quantum Dot. *J. Am. Chem. Soc.* **2012**, *134*, 5577–5585.

(5) Katayama-Yoshida, H.; Sato, K. Spin and charge control method of ternary II–VI and III–V magnetic semiconductors for spintronics: theory vs. experiment. *J. Phys. Chem. Solids* **2003**, *64*, 1447–1452.

(6) Schimpf, A. M.; Ochsenbein, S. T.; Gamelin, D. R. Surface contributions to Mn^{2+} spin dynamics in colloidal doped quantum dots. *J. Phys. Chem. Lett.* **2015**, *6* (3), 457–463.

(7) Fainblat, R.; Barrows, C. J.; Hopmann, E.; Siebeneicher, S.; Vlaskin, V. A.; Gamelin, D. R.; Bacher, G. Giant Excitonic Exchange Splittings at Zero Field in Single Colloidal CdSe Quantum Dots Doped with Individual Mn^{2+} Impurities. *Nano Lett.* **2016**, *16* (10), 6371–6377.

(8) Liang, B. B.; Hou, L. P.; Zou, S. Y.; Zhang, L.; Guo, Y. C.; Liu, Y. T.; Farooq, M. U.; Shi, L. J.; Liu, R. B.; Zou, B. S. The aggregation of Fe^{3+} and their d–d radiative transitions in ZnSe: Fe^{3+} nanobelts by CVD growth. *RSC Adv.* **2018**, *8* (6), 3133–3139.

(9) Xie, R.; Li, Y.; Jiang, L.; Zhang, X. Insights into the microstructural and physical properties of colloidal Fe: ZnSe nanocrystals. *Appl. Surf. Sci.* **2014**, *317*, 469–475.

(10) Kulyuk, L. L.; Laiho, R.; Lashkul, A. V.; Lähderanta, E.; Nedeoglo, D. D.; Nedeoglo, N. D.; Radevici, I. V.; Siminel, A. V.; Sirkeli, V. P.; Sushkevich, K. D. Magnetic and luminescent properties of iron-doped ZnSe crystals. *Phys. B* **2010**, *405* (20), 4330–4334.

(11) Laiho, R.; Lashkul, A. V.; Lähderanta, E. M.; Nedeoglo, D. D.; Nedeoglo, N. D.; Radevici, I. V.; Sirkeli, V. P.; Sushkevich, K. D.; Ferro, G.; Siffert, P. Magnetic Properties of ZnSe Crystals doped with Transition Metals. *AIP Conf. Proc.* **2010**, *1292* (1), 197–200.

(12) Godlewski, M.; Surma, M.; Ivanov, V. Y.; Surkova, T. P. Mechanisms of radiative and nonradiative recombination in ZnSe: Cr and ZnSe: Fe. *Low Temp. Phys.* **2004**, *30*, 891–896.

(13) Xie, R.; Li, Y.; Zhang, X.; Liu, H. Low-cost, environmentally friendly synthesis, structural and spectroscopic properties of Fe: ZnSe colloidal nanocrystals. *J. Alloys Compd.* **2015**, *621*, 396–403.

(14) Tomiyasu, K.; Kamazawa, K. A spin molecule model for geometrically frustrated spinel $ZnFe_2O_4$. *J. Phys. Soc. Jpn.* **2011**, *80*, SB024.

(15) Karmakar, D.; Mandal, S. K.; Kadam, R. M.; Paulose, P. L.; Rajarajan, A. K.; Nath, T. K.; Das, A. K.; Dasgupta, I.; Das, G. P. Ferromagnetism in Fe-doped ZnO nanocrystals: experiment and theory. *Phys. Rev. B: Condens. Matter Mater. Phys.* **2007**, *75*, 144404.

(16) Singh, S. B.; Limaye, M. V.; Date, S. K.; Gokhale, S.; Kulkarni, S. K. Iron substitution in CdSe nanoparticles: magnetic and optical properties. *Phys. Rev. B: Condens. Matter Mater. Phys.* **2009**, *80* (23), 235421.

(17) Bui, D. H.; Phan, V. N. Ferromagnetic clusters induced by a nonmagnetic random disorder in diluted magnetic semiconductors. *Ann. Phys.* **2016**, *375*, 313–321.

(18) Gutsev, L. G.; Dalal, N. S.; Maroulis, G.; Gutsev, G. L. Structure and magnetic properties of $Cd_{9-n}Se_9Mn_n$ and $Cd_{9-n}Se_9$ Fe_n clusters (n = 0 − 9). *Chem. Phys.* **2016**, *469*, 105–114.

(19) Rudra, I.; Wu, Q.; Van Voorhis, T. Predicting exchange coupling constants in frustrated molecular magnets using density functional theory. *Inorg. Chem.* **2007**, *46* (25), 10539–10548.

(20) Hu, Y.; Ji, C.; Wang, X.; Huo, J.; Liu, Q.; Song, Y. The structural, magnetic and optical properties of TM n@$(ZnO)_{42}$ (TM= Fe, Co and Ni) hetero-nanostructure. *Sci. Rep.* **2017**, *7* (1), 16485.

(21) Nguyen, K. A.; Day, P. N.; Pachter, R. Understanding structural and optical properties of nanoscale CdSe magic-size quantum dots:

DOI: 10.1021/acs.chemmater.8b00143
Chem. Mater. 2018, 30, 2093–2101

insight from computational prediction. *J. Phys. Chem. C* **2010**, *114* (39), 16197−16209.
(22) Michel, A.; Balkanski, M. *Semimagnetic semiconductors and diluted magnetic semiconductors*; Springer Science & Business Media: 2012; Vol. *55*.
(23) Foley, M. E.; Meulenberg, R. W.; McBride, J. R.; Strouse, G. F. Eu^{3+}-Doped ZnB_2O_4 (B = Al^{3}+, Ga^{3+}) nanospinels: an efficient red phosphor. *Chem. Mater.* **2015**, *27* (24), 8362−8374.
(24) Diep, H. T. *Frustrated spin systems*; World Scientific: 2013; DOI: 10.1142/8676
(25) Cumberland, S. L.; Hanif, K. M.; Javier, A.; Khitrov, G. A.; Strouse, G. F.; Woessner, S. M.; Yun, C. S. Inorganic clusters as single-source precursors for preparation of CdSe, ZnSe, and CdSe/ZnS nanomaterials. *Chem. Mater.* **2002**, *14* (4), 1576−1584.
(26) Zhou, D.; Kittilstved, K. R. Control over Fe^{3+} speciation in colloidal ZnO nanocrystals. *J. Mater. Chem. C* **2015**, *3* (17), 4352−4358.
(27) Singhal, A.; Achary, S. N.; Manjanna, J.; Jayakumar, O. D.; Kadam, R. M.; Tyagi, A. K. Colloidal Fe-doped indium oxide nanoparticles: facile synthesis, structural, and magnetic properties. *J. Phys. Chem. C* **2009**, *113* (9), 3600−3606.
(28) Watanabe, H. g-value of Fe3+ in II−VI cubic crystals. *J. Phys. Chem. Solids* **1964**, *25* (12), 1471−1475.
(29) Zhou, D.; Kittilstved, K. R. Electron trapping on Fe^{3+} sites in photo doped ZnO colloidal nanocrystals. *Chem. Commun.* **2016**, *52* (58), 9101−9104.
(30) Binder, K.; Young, A. P. Spin glasses: Experimental facts, theoretical concepts, and open questions. *Rev. Mod. Phys.* **1986**, *58* (4), 801−976.
(31) Magana, D.; Perera, S. C.; Harter, A. G.; Dalal, N. S.; Strouse, G. F. Switching-on superparamagnetism in Mn/CdSe quantum dots. *J. Am. Chem. Soc.* **2006**, *128* (9), 2931−2939.
(32) Carlin, R. L. *Magnetochemistry*; Springer Science & Business Media: 2012.
(33) Mørup, S.; Dumesic, J. A.; Topsøe, H. *Applications of Mössbauer Spectroscopy*; Academic Press: 1980; pp 1−53.
(34) Gütlich, P.; Bill, E.; Trautwein, A. X. *Mössbauer Spectroscopy and Transition Metal Chemistry*; Springer-Verlag: 2011.
(35) Dickson, D. Mössbauer studies of biological nanophase magnetic materials. *Hyperfine Interact.* **1998**, *111*, 171−177.
(36) Mörup, S.; Tronc, E. Superparamagnetic relaxation of weakly interacting particles. *Phys. Rev. Lett.* **1994**, *72*, 3278−3281.
(37) Hansen, M.; Mörup, S. Models for the dynamics of interacting magnetic nanoparticles. *J. Magn. Magn. Mater.* **1998**, *184*, L262−274.
(38) Bochevarov, A. D.; Friesner, R. A.; Lippard, S. J. Prediction of ^{57}Fe Mossbauer Parameters by Density Functional Theory: A Benchmark Study. *J. Chem. Theory Comput.* **2010**, *6* (12), 3735−3749.
(39) Partridge, H. Near Hartree−Fock quality GTO basis sets for the first-and third-row atoms. *J. Chem. Phys.* **1989**, *90* (2), 1043−1047.
(40) Morley, G. W.; Brunel, L. C.; van Tol, J. A multifrequency high-field pulsed electron paramagnetic resonance/electron-nuclear double resonance spectrometer. *Rev. Sci. Instrum.* **2008**, *79* (6), 064703.
(41) Van Tol, J.; Brunel, L.-C.; Wylde, R. J. A quasioptical transient electron spin resonance spectrometer operating at 120 and 240 GHz. *Rev. Sci. Instrum.* **2005**, *76*, 074101.
(42) Rancourt, D. G.; Ping, J. Y. Voigt-based methods for arbitrary-shape static hyperfine parameter distributions in Mössbauer spectroscopy. *Nucl. Instrum. Methods Phys. Res., Sect. B* **1991**, *58*, 85.
(43) Frisch, M. J.; Trucks, G. W.; Schlegel, H. B.; Scuseria, G. E.; Robb, M. A.; Cheeseman, J. R.; Scalmani, G.; Barone, V.; Mennucci, B.; Petersson, G. A.; Nakatsuji, H.; Caricato, M.; Li, X.; Hratchian, H. P.; Izmaylov, A. F.; Bloino, J.; Zheng, G.; Sonnenberg, J. L.; Hada, M.; Ehara, M.; Toyota, K.; Fukuda, R.; Hasegawa, J.; Ishida, M.; Nakajima, T.; Honda, Y.; Kitao, O.; Nakai, H.; Vreven, T.; Montgomery, J. A., Jr.; Peralta, J. E.; Ogliaro, F.; Bearpark, M.; Heyd, J. J.; Brothers, E.; Kudin, K. N.; Staroverov, V. N.; Kobayashi, R.; Normand, J.; Raghavachari, K.; Rendell, A.; Burant, J. C.; Iyengar, S. S.; Tomasi, J.; Cossi, M.; Rega, N.; Millam, J. M.; Klene, M.; Knox, J. E.; Cross, J. B.; Bakken, V.; Adamo, C.; Jaramillo, J.; Gomperts, R.; Stratmann, R. E.; Yazyev, O.; Austin, A. J.; Cammi, R.; Pomelli, C.; Ochterski, J. W.; Martin, R. L.; Morokuma, K.; Zakrzewski, V. G.; Voth, G. A.; Salvador, P.; Dannenberg, J. J.; Dapprich, S.; Daniels, A. D.; Farkas, O.; Foresman, J. B.; Ortiz, J. V.; Cioslowski, J.; Fox, D. J. *Gaussian 09*; Gaussian, Inc.: Wallingford, CT, 2009.
(44) Becke, A. D. Density-functional exchange-energy approximation with correct asymptotic behavior. *Phys. Rev. A: At., Mol., Opt. Phys.* **1988**, *38* (6), 3098.
(45) Perdew, J. P.; Wang, Y. Accurate and simple analytic representation of the electron-gas correlation energy. *Phys. Rev. B: Condens. Matter Mater. Phys.* **1992**, *45* (23), 13244.
(46) Curtiss, L. A.; McGrath, M. P.; Blaudeau, J. P.; Davis, N. E.; Binning, R. C., Jr; Radom, L. Extension of Gaussian-2 theory to molecules containing third-row atoms Ga−Kr. *J. Chem. Phys.* **1995**, *103* (14), 6104−6113.
(47) Weigend, F.; Ahlrichs, R. Balanced basis sets of split valence, triple zeta valence and quadruple zeta valence quality for H to Rn: Design and assessment of accuracy. *Phys. Chem. Chem. Phys.* **2005**, *7* (18), 3297−3305.
(48) Partridge, H. Near Hartree−Fock quality GTO basis sets for the first-and third-row atoms. *J. Chem. Phys.* **1989**, *90* (2), 1043−1047.

DOI: 10.1021/acs.chemmater.8b00143
Chem. Mater. 2018, 30, 2093−2101